Contents list available at CBIORE website

International Journal of Renewable Energy Development

Journal homepage: https://ijred.cbiore.id

Research Article

CFD analysis of key factors impacting the aerodynamic performance of the S830 wind turbine airfoil

Le Thi Tuyet Nhung*, Nguyen Van Y, Dinh Cong Truong, Vu Dinh Quy

School of Mechanical Engineering, Hanoi University of Science and Technology, Hanoi, Vietnam

Abstract. The Global Wind Energy Council (GWEC) reported that in 2021, global wind capacity increased by 93.6 GW (+12%), reaching a total of 837 GW, most of which was contributed by wind turbines. Improving wind turbine performance primarily hinges on advancements in blade technology and airfoil design. This study examines the effect of profile thickness on the aerodynamic performance of the S830 airfoil at a Reynolds number of 25,148, as part of the NREL airfoil's aerodynamic performance research. However, the impacts of additional variables—such as angle of attack, Reynolds number, speed range, and particularly ice accretion—have not been thoroughly investigated. This study utilized a 2D CFD model provided by the commercial software ANSYS Fluent and FENSAP-ICE. The lift-to-drag ratio of the S830 wind turbine airfoil was examined, considering the effects of angle of attack, wind speed, Reynolds number, airfoil thickness, and ice accretion. Additionally, design-related solutions will be suggested. The research indicates that the optimal angle of attack increases the lift-to-drag ratio by approximately 250% compared to a zero angle of attack. An increase in wind speed causes this coefficient to rise nonlinearly within the studied velocity range. The Reynolds number directly influences the optimal angle of attack. According to CFD results, the lift-to-drag ratio can be increased by 50% if the airfoil's thickness is reduced by 20% compared to the original profile. For the ice accretion simulation model, a case test of the NACA 0012 airfoil was conducted to verify the model's parameters. Subsequently, a survey of this phenomenon on the S830 airfoil revealed that the lift coefficient decreased by 5.25% after 90 minutes of ice accretion.

Keywords: Airfoil S830, wind turbine performance, CFD, Reynold number, ice accretion

Received: 27th April 2024; Revised: 18th July 2024; Accepted: 26th Sept 2024; Available online: 4th Oct 2024

1. Introduction

Improving wind turbine efficiency is a real problem that many design engineers and leading organizations in the world have been aiming for in recent years. For example, NASA spent 20 years from 1976 to 1996 developing and researching wind turbines, with 14 models launched to help shape the wind energy industry today. In particular, the goal of developing technology to manufacture blades is given top priority because this is the first part directly involved in converting wind energy into kinetic energy to operate a generator. A good wing structure will provide optimal wind extraction efficiency.

In recent years, the world has recorded many scientific publications by individuals and organizations, contributing to the introduction of new research methods and applications. Typically, studies provide numerical solutions to aerodynamically related wing configuration optimization problems. An article studied wind turbine airfoil performance at low speed when changing airfoil thickness in aerodynamic simulation using commercial software ANSYS. Research shows that thinner airfoils will give a larger coefficient of lift, similar to when comparing different wind turbine airfoils, including airfoil S830 (Abdulkareem *et al.,* 2021). For the S830 airfoil, using the Blade Element Momentum (BEM) method, the suitable blade size is 56 meters for a 1 MW wind turbine and 0.8 meters for a 100 W turbine (Velázquez *et al.,* 2014). The study of airfoil performance towards the influence of Reynolds number provides an overview of the study method on the influence of fluid environment properties and the size of the airfoil bowstring (Shah *et al.,* 2012).The variation of turbine efficiency with blade angle and wind speed has been shown to be closely related to the entropy generation of the airfoil, which is shown in the result numerically (Mamouri *et al.*, 2019). The influence of other factors on performance in the environment is also thoroughly studied. The NASA Lewis Icing Research Tunnel's ice accretion experiment (Jaiwon Shin and Thomas H. Bond, 1992) demonstrates good controllability of circumstances to explore this phenomenon for the parameters of diameter droplet and liquid water content (LWC). Studies conducted by Virk (Virk *et al.*, 2010) demonstrate how ice accretion affects the airfoil's aerodynamic performance. Specifically, the tape reduces the lift-to-drag ratio C_L/C_D by 7–10% and alters the curve shape of the lift coefficient (C_L), drag coefficient (C_D), and stall angle. A study that used profile integration theory and B-spline functions to optimize the trailing edge geometry under freezing conditions produced encouraging results. The result is the new airfoil NACA0012BT, which has been shown to fully meet the optimal requirements (Zhang *et al.*, 2022). Rain, another common weather phenomenon, has also been studied. The study concludes with a significant decrease in the C_L/C_D ratio, with a maximum reduction of 48% and an average reduction of 31%. These results are remarkably similar to the earlier empirical model by Hansman and Barsotti, as described in the text (Cai *et*

* Corresponding author
Email: nhung.lethituyet@hust.edu.vn (L.T.T. Nhung)

https://doi.org/10.61435/ijred.2024.60249
ISSN: 2252-4940/© 2024.The Author(s). Published by CBIORE

al., 2012). In 2016, a study replicated this work under different conditions for liquids, including flow, raindrop kinetic energy, and surface wetting angle. The results demonstrated significant performance fluctuations between cases (Cohan *et al.*, 2016). All of the research mentioned above utilized 2D models and commercial software such as ANSYS and X-Foil. The 3D model research is focused on the aerodynamic applications of the turbine blade. A research paper examined slotted airfoil aerodynamic properties using a turbine model. The findings indicate that the potential to lower the wing pattern's efficiency would be significantly impacted by the scientifically developed groove position (Belamadi *et al.*, 2016). Research on wind turbine aerodynamic brake design utilizing a 3D model has shown that slotted brakes are highly effective, reducing the C_L/C_D ratio by up to 40% and decreasing the torque on the 3D wings by 30% (Navin Kumar *et al.*, 2020). Other studies on vortex generators were also conducted. The velocity streamlines in the investigation demonstrated that vortex generators significantly reduced flow separation on the airfoil surface, especially at large angles of attack (Mereu *et al.,* 2019). Further research into the efficiency of wind turbine blades involved applying blade twist and Blade Element Momentum (BEM) theory. The findings demonstrate that the untwisted wing produces greater torque than the twisted wing; the difference grows as wind speed increases, reaching 13% at 12 m/s (Mohamed *et al.*, 2015), and additional experimental findings support this distinction (Mohamed *et al.*, 2021). Noise from wind turbines is also a significant concern. A study on a novel Serrated Gurney Flap (SGF) demonstrated that the ASGF-0.8–6.7 configuration reduced noise by 10.2 dB compared to no flap usage. Furthermore, according to Ye *et al.* (2023), the technique helps reduce the angle of attack to 3 degrees and increases the lift-to-drag ratio by 8.61%. The results of the experimental study on noise produced by cracked airfoils at the trailing edge show that noise levels increase with the size of the crack. However, differences in noise between cracks diminish with changes in the angle of attack or variations in input disturbance (Zhang *et al.,* 2022). Designing shapes to affect noise elements is also considered. Research on the J-shaped wind turbine indicates that this new type only reduces performance without reducing noise (Mohamed, 2019). There is a correlation between airfoil thickness and noise, as demonstrated by research findings. In particular, the thickness of the airfoils significantly influences the creation of tonal noise and its frequency characteristics (Geyer *et al.*, 2021). Research using a holistic approach indicates that concave serrations provide the best overall performance in reducing noise discomfort. It has been noted that the sound properties of wind turbine noise, including tone, spectral content, and amplitude modulation, are significant factors in inducing unpleasant emotions (Merino-Martínez *et al.*, 2021). The literature review includes studies on optimization frameworks for wind turbine blades. Notably, a genetic algorithm for evaluating structural integrity was adopted by Sang-Lae Lee *et al.* (2021). J. A. Orosa et al. illustrate the viability of using a nozzle wind concentrator in Galicia in various seasonal climate conditions, where the density of the moist air varies due to its relative humidity (J. A. Orosa *et al.*, 2012). An investigation into failures occurring during the start-up and braking phases of a 1.5 MW horizontal-axis wind turbine blade was conducted using both a measured wind field and fluid-structure interaction techniques (Kangqi Tian *et al.*, 2021). This comprehensive study utilizes the Autoregressive Distributed Lag (ARDL) model to analyze the impact of renewable energy, CO2 emissions, currency exchange rates, and economic development in Bangladesh, India, Pakistan, and Sri Lanka (Rahman *et al.*, 2023). Guenoupkati proposes a method for modeling wind speed data in the West African region using combinations of Weibull distributions (Guenoupkati *et al.,* 2023). A recent study focuses on the development and evaluation of a 3D-printed micro-wind turbine system designed to generate electricity for homes. The researchers chose to create a three-dimensional CFD model to simulate the micro-wind turbine (Shalby *et al.*, 2023). By combining the turbulent model and the ANSYS FLOTRAN CFD solver, which is based on RANS theory, with the structural equations, Rana et al. were able to simulate the time domain of airfoil flutter (Rana *et al.*, 2009). Approximately ten years ago, research was conducted on the impact of blade vibration on the dynamic stall characteristics of a large-scale horizontal-axis wind turbine (HAWT) blade (Liu *et al.*, 2015). Evaluating aerodynamic loads on the blade surface across wind speeds ranging from 4 m/s to 24 m/s, the study concluded that the wind turbine could likely operate for 20 years before experiencing fatigue from bending moments. Additionally, Horcas *et al.* (2022) examined the use of a trailing edge flap to mitigate vortex-induced vibrations on a 96-meter-long wind turbine blade at standstill, integrating a CFD model with a multi-body structural solver. They verified the CFD and FSI techniques, but an experiment is still required to corroborate their findings. Thi-Hong-Hieu Le *et al.* (2023) highlighted the advantages of the transition k-SST turbulence model compared to the standard k-SST turbulence model. The turbulence model k-ω SST accurately simulated the dynamic pulsation of the 2D S809 tower-blade (Tzong-Hann Shieh *et al.,* 2016). In their investigation of the flutter behavior of 20 kW horizontal-axis wind turbine (HAWT) blades at varying wind speeds, Le T.T.N. *et al.* used composite epoxy-glass material for the layup structure and balsa wood for the sandwich core to determine the flutter velocity (Le *et al.*, 2022). The CFD simulation of these HAWTs was used to calculate the input loads for the construction and durability analysis of the turbine tower structure. The ICE standard 61400 was applied to assess the wave and aerodynamic loads acting on the tower's pier (Vu *et al.*, 2022). CFD simulations using URANS theory and the SST turbulence model were employed to analyze the random vibration fatigue of composite wind turbine blades. An exponential decline in fatigue life was observed for the Normal Turbulence Model scenario across a wide range of wind velocities, from 6 m/s to 25 m/s (Le *et al.*, 2023). To assess the wind energy output of an offshore wind farm, four models—Jensen, Larsen, Ishihara, and Frandsen—were applied to predict the behavior of aligned and misaligned wakes across a row of ten turbines (Hassoine *et al.*, 2022). Additionally, Ghiasi *et al.* (2021) investigated the performance of the H-type Darrieus wind turbine using a double multiple stream tube (DMST) model and a two-dimensional computational fluid dynamics (CFD) simulation. In their CFD analysis, they utilized the Unsteady Reynolds Averaged Navier-Stokes (URANS) equations and applied the SST k-ω model for solving them. Beabpimai *et al.* (2019) investigated how changes in blade twist affect the aerodynamic performance of wind turbine rotors using CFD techniques. Meanwhile, Mrigua *et al.* (2020) conducted a numerical study to explore how the number of stages influences the efficiency of a Savonius wind turbine, employing a 3D numerical simulation with the SST k-ω turbulence model. Given that it may be employed at both low and high-speed ranges, the S 830 airfoil was selected as the subject of study in order to address the design requirements for small and medium-sized turbines for Vietnam's mountainous regions. Among the studies previously mentioned, Abdulkareem *et al.* (2021) investigated how profile thickness affects the aerodynamic performance of the Airfoil S 830 at a Reynolds number of 25,148. The effects of additional factors, such as angle of attack, Reynolds number, and speed range, have not yet been fully explored. To design a

wind turbine suitable for highland areas in Vietnam, like Sapa, where the cold climate can bring snow, it is essential to study various weather conditions.

2. Materials and methods

This study aimed to optimize the aerodynamic performance of the S 830 airfoil cross-section through two CFD and ice accretion simulation models. The first step involved using CFD simulations to determine the 2D parameters for optimal aerodynamic performance. In this phase, the original CFD simulation results were established and verified for accuracy. Simultaneously, the effects of the angle of attack, wind speed, Reynolds number, and airfoil thickness on aerodynamic performance were analyzed. The next step was to simulate ice formation on the wing. Using ANSYS FENSAP-ICE and FLUENT, the impact of ice accretion on the aerodynamic characteristics of the S 830 airfoil was examined. Additionally, NASA's Case Test was conducted to validate the reliability of the ice formation simulation model (Jaiwon Shin *et al.,* 1992). Finally, an analysis of the ice accretion phenomenon on the S 830 airfoil was performed under SAPA case conditions.

2.1 Airfoil selection.

The airfoil selected for the study is the airfoil S830 of the airfoil NREL family (Figure1). The NREL airfoils integrated into the turbine blades have been extensively tested, demonstrating their outstanding performance. The airfoil represents a significant technical innovation in wind technology over the past decade. This article will examine the NREL S830 airfoil to compare its performance under various environmental conditions. In the NREL family of airfoils, the three most common ones are S 830, SD7062 and SG6043. The last two types, SD 7062 and SG6043, are commonly used at low wind speeds. The S830, one of the most efficient profiles from NREL, is selected due to its suitability for wind turbines operating across a range of wind speeds, both high and low.

2.2 Numerical analysis.

CFD simulations were conducted using commercial software to explore the impact of angle of attack and wind speed ranges.

The solver parameters used include steady, incompressible, and pressure-based solvers in ANSYS FLUENT. The governing equations employed are the continuity equation and the Navier-Stokes equations, as cited in Abdulkareem *et al.* (2021).

$$\frac{\partial u}{\partial u}+\frac{\partial v}{\partial y}=0 \quad (1)$$

X-direction flow:

$$\rho\left(u\frac{\partial u}{\partial x}+v\frac{\partial u}{\partial y}\right)=-\frac{\partial p}{\partial x}+\left(\frac{\partial^2 u}{\partial u^2}+\frac{\partial^2 u}{\partial y^2}\right) \quad (2)$$

Y-direction flow:

$$\rho\left(u\frac{\partial v}{\partial x}+v\frac{\partial v}{\partial y}\right)=-\frac{\partial p}{\partial y}+\left(\frac{\partial^2 v}{\partial x^2}+\frac{\partial^2 v}{\partial y^2}\right) \quad (3)$$

The C_L and C_D values are calculated by ANSYS Fluent using the following equations:

$$C_L=\frac{L}{\frac{1}{2}\rho U^2 C\, l} \quad (4)$$

$$C_D=\frac{D}{\frac{1}{2}\rho U^2 C\, l} \quad (5)$$

The Spalart-Allmaras turbulence model was selected for the computation because wind turbines usually operate within a low wind speed range of 5 to 20 m/s. This model is well-suited for low-speed flows and is advantageous due to its fast computation, requiring only a single parameter. The behavior of the Spalart-Allmaras model is similar to that of turbulent kinematic viscosity, though it differs in regions influenced by viscosity (Abdulkareem *et al.*, 2021).

The dynamic equation for the variable chaotic viscosity is:

$$\frac{\partial}{\partial t}(\rho\tilde{\nu})+\frac{\partial}{\partial x_i}(\rho\tilde{\nu}u_i)$$

$$=G_v+\frac{1}{\sigma_{\tilde{\nu}}}\left[\frac{\partial}{\partial x_j}\left\{(\mu+\rho\tilde{\nu})\frac{\partial\tilde{\nu}}{\partial x_j}\right\}+C_{b2}\rho\left(\frac{\partial\tilde{\nu}}{\partial x_j}\right)^2\right]-Y_v+S_{\tilde{\nu}} \quad (6)$$

When moving particles of supercooled water (below 0◦C) collide and adhere to the walls of the interacting surface, a phenomenon known as ice accretion occurs. Consequently, the project's study and application focus on wind turbines situated in cold areas with high humidity levels, which can lead to the condensation of minuscule water particles in the atmosphere or the formation of clouds on the surface of airplane wings at high altitudes. In relation to the theory of calculating the ice accretion rate, Makkonen's equation is stated as follows (Makkonen et al. 2018):

$$\frac{dM}{dt}=\alpha_1.\alpha_2.\alpha_3.wvA \quad (7)$$

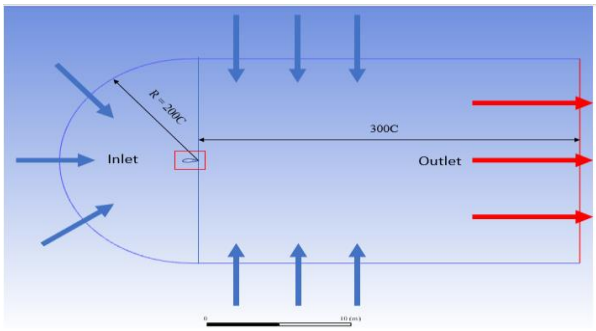

Fig. 1 Fluid domain dimension

Table 1
Influence of mesh size.

No. of Element	C_D	C_L	Difference of C_D (%)	Difference of C_L (%)
47.000	0.00389	0.02554	--------	--------
194.000	0.00386	0.02398	0.759981	6.095632
437.700	0.00385	0.02312	0.288715	3.599546
776.000	0.00384	0.02232	0.226325	3.436397
1.154.000	0.00384	0.02232	0.017318	0.015371

Table 2
Boundary set up

Mesh	C-grid, No. of element: 776,000.
Turbulence	*Spalart-Allmaras model.*
Fluid	Air density 1.225 kg/m^3, viscosity 1.7894e-05 Kg/(m.s).
Method	Second order accuracy, pressure–velocity coupling
Convergence criteria	Less than 10e-5.
Boundary conditions	Velocity inlet, Pressure outlet *Turbulence intensity*: 5%. *Airfoil*: Wall, no slip.

The surface's cross-sectional area (m^2) is denoted by A. The wind speed v is measured in meters per second (m/s). The liquid water content (LWC) in the flow, expressed in kilograms per cubic meter (kg/m^3), is represented by w. The rate of ice accretion, given in kilograms per second (kg/s), is denoted as dM/dt. The collision coefficient is denoted by α_1. Adhesion coefficient is denoted by α_2. The coefficient of accretion is α_3.

2.3 Model and meshing.

Using the airfoil tool, the airfoil profile is exported as discrete points. These points are then connected using 2D and 3D drawing software to create the complete airfoil shape. In ANSYS's Design Modeler tool, these points are used to generate the airfoil S830 with a chord length of C=0.09 m based on the numerical simulation engine. After defining the airfoil shape, the liquid domain (air) parameter is specified. The fluid domain for the airfoil is represented by the C-shaped mesh shown in Figure 2. The C-shaped section will be positioned at the leading edge of the airfoil, facilitating easier meshing with software such as ANSYS Meshing or ICEM. The dimensions of the liquid domain are as follows: C-zone radius is 200 times the chord length (200C), and the length of the liquid domain from the trailing edge is 300 times the chord length (300C).

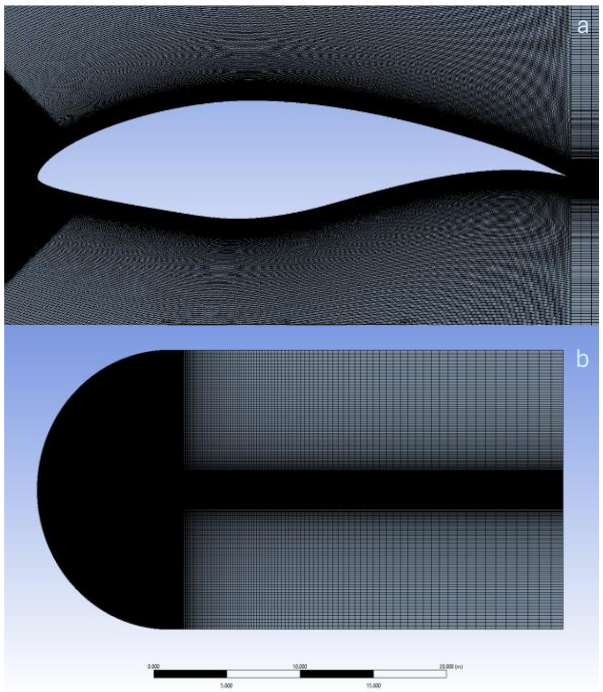

Fig. 2 Airfoil mesh (a) and Fluid domain mesh (b)with No. of element 776,000

Grid size plays a crucial role in the accuracy of CFD calculations. The article will divide and calculate with four grid sizes to find out the grid error and conclude the optimal grid. With an angle of attack of 0 degrees and a wind speed of 5 m/s, the boundary conditions are consistent across all four grids.
Table 1 illustrates the influence of mesh size on simulation results. As the grid size increases, the errors in C_L and C_D gradually approach zero. When the number of elements in the grid reaches approximately 776,000 to 1,154,000, the error between different runs becomes very small, around 0.01% to 0.02%. Therefore, a grid with 776,000 elements ensures both the accuracy and computational efficiency of the model. Figures 2a and 2b display the grid. Under the conditions specified in Table 2, this grid is used to develop the model. Turbulence intensity is typically categorized as low (1%), medium (5%), or high (10%). In this case, a medium turbulence intensity of 5% is selected.

3. Results and discussion.

3.1 Effect of angle of attack.

One of the primary factors affecting the airfoil's aerodynamic performance is the angle of attack. Compared to scenarios without an angle of attack, the C_L/C_D ratio can be significantly improved with an optimal angle of attack. This improvement occurs because the angle of attack affects the pressure difference between the top and bottom surfaces of the airfoil, thereby influencing the C_L/C_D ratio. The simulation results illustrate the relationship between the angle of attack and the C_L/C_D coefficient. To explore various angles of attack, the wind speed in the simulation is adjusted by varying the velocity values along the X and Y axes. This method facilitates faster problem resolution by eliminating the need to re-grid the model for each angle of attack, thus streamlining the simulation process. The Figure 3 shows the results of the simulation using the baseline airfoil S830 and a wind speed of 5 m/s.

Figure 3 shows that as the angle of attack increases, the lift-to-drag ratio (C_L/C_D) initially rises. However, once the angle of attack exceeds the optimal value, the C_L/C_D ratio begins to decrease. This occurs because, as the angle of attack approaches its critical limit, flow separation occurs over the airfoil. This separation leads to a loss of lift and a continuous increase in drag due to the airfoil's shape. This happens because the pressure difference between the top and bottom surfaces of the airfoil remains relatively constant as the angle of attack increases. As the angle of attack continues to rise, the drag increases due to the increasing component of the airfoil's profile in the Y direction. The aerodynamic coefficient C_L/C_D increased from 5.74 at a 0-degree angle of attack to a peak value of 14.53

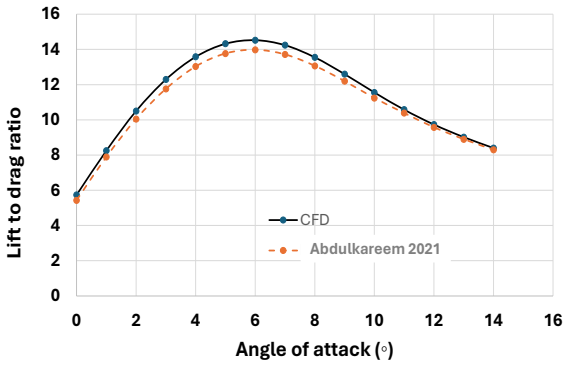

Fig. 3. CFD result and Abdulkareem's result

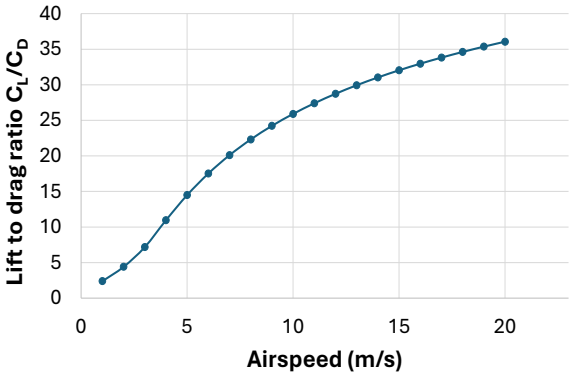

Fig. 5 Lift to drag ratio vs Air speed

at a 6-degree angle of attack, before slightly decreasing to 8.3 at 14 degrees. The maximum error between this study's simulation and Abdulkareem's (2021) study is 3.8% at the optimal angle of attack of 6 degrees, indicating the reliability of the simulation results.

Figures 4a and 4b illustrate the velocity distribution around the S830 wing profile at 6 and 14 degrees of attack, respectively. At 6 degrees, flow separation occurs later, at 56% of the chord, while at 14 degrees, it begins earlier at 37.5% of the chord. This early separation at higher angles of attack accounts for the drop in aerodynamic efficiency when the angle of attack surpasses the optimal 6 degrees. The initial simulation results indicate that within the allowable range, a 6-degree angle of attack is the optimal angle for the S830 airfoil. Consequently, when analysing the effects of other parameters, such as velocity and Reynolds number, the 6-degree angle of attack is used as the reference.

3.2 Effect of wind velocity.

The second scenario examined is the impact of wind speed on the coefficient C_L/C_D. Since both the C_L and C_D systems depend on the air velocity or the airfoil travel velocity, the C_L/C_D coefficient will also change with different velocities. The graph of the coefficient of C_L/C_D with velocity is not linear but has the form of a curve going up to the limit and going down (Gudmundsson 2014). Because the critical velocity of the airfoil is usually very high, it can be said that it is outside the airfoil's operating area, so this article will only consider the speed range of 0–20 m/s to match the angle of attack of 6. Figure 5 illustrates the change in the aerodynamic quality coefficient of the S830 profile as the speed increases from 1 m/s to 20 m/s. The coefficient rises steadily within the speed range of 1 to 7 m/s (from 2.38 to 20) and then increases more gradually as the speed reaches 20 m/s, where it reaches a value of 36.05.

3.3 Effect of Reynold number.

The Reynolds number represents a relationship that is proportional to linear size (flow scale) velocity, density, and inversely proportional to viscosity. Thus, a higher Reynolds number is associated with an increase in flow velocity under the same flow conditions. The same principle applies to other parameters. Therefore, the effect of changing the Reynolds number from 15,000 to 100,000 on aerodynamic performance was examined. The results of these simulations are presented in Figure 6. As the Reynolds number increases from 15,000 to 100,000, the aerodynamic quality coefficient increases approximately fivefold (from 7.2 to 35.97). At lower Reynolds numbers, the aerodynamic coefficient shows minimal variation, but the changes become more pronounced as the Reynolds number rises. Additionally, the optimal angle of attack shifts within the range of 5 to 7 degrees. As seen in Figure 6, the ideal airfoil angles of attack for every Reynolds plot line are indicated by an X. It can be observed that as Reynolds number increases

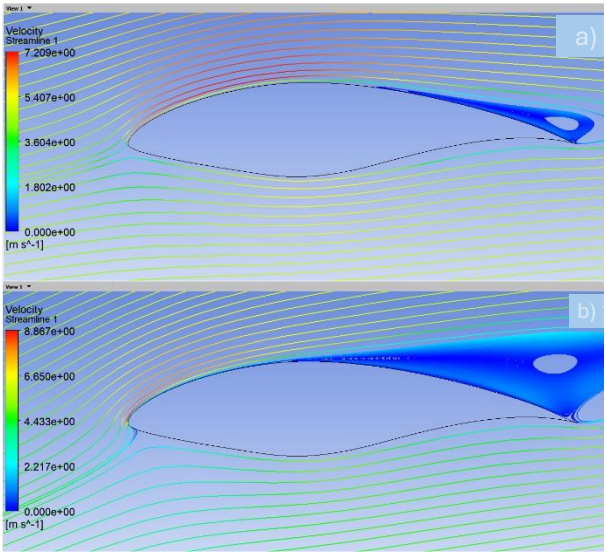

Fig. 4 Streamline air velocity in airfoil a) AoA 6◦, b) AoA 14◦

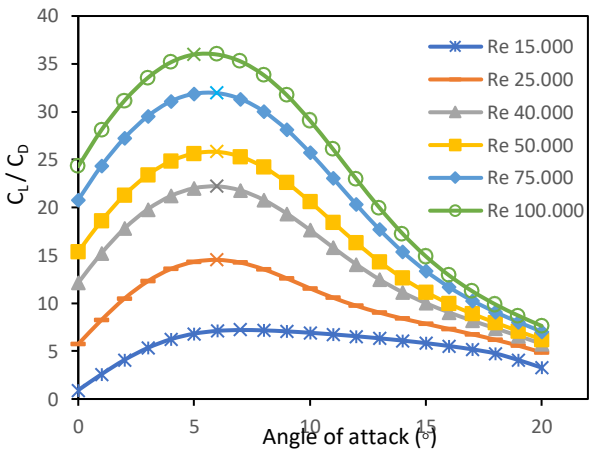

Fig. 6 Lift to drag ratio vs AoA and Reynold number

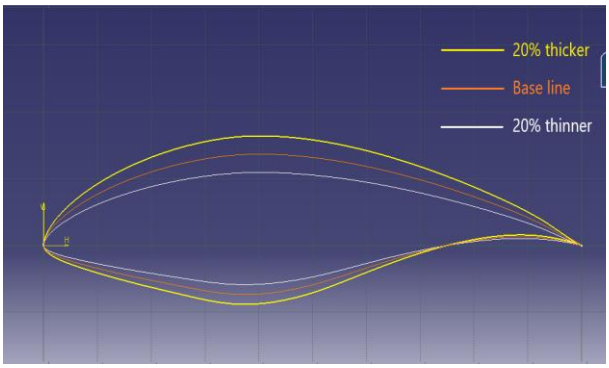

Fig. 7 Airfoil S830 with different thickness

(by increasing the velocity while keeping other flow parameters constant), the optimal angle of attack gradually shifts towards 0 degrees. The same is pointed out in the scientific publication (Shah *et al.,* 2012).

3.4 Effect of thickness.

The thickness size change from the original airfoil is a 20% increase in thickness and a 20% decrease in thickness; this is simply done with the calculator or the airfoil tool website Xfoil (Shah *et al.,* 2012). The size of the airfoil after the change is shown in Figure 7.

Figure 8a presents the simulation results for three different thicknesses and angles of attack under the same atmospheric conditions mentioned earlier. The obtained C_L/C_D values are compared with the findings of Abdulkareem *et al.* (2021) to verify accuracy. In the case of a 20% reduction in thickness, the aerodynamic quality factor improves by 41.4% (rising from 14.5 to 20.5). Conversely, for a 20% increase in thickness, the aerodynamic quality factor drops by 48,7% (from 14.5 to 7.43). When compared to Abdulkareem et al.'s results, the errors for these two cases are 1% and 5%, respectively. The results

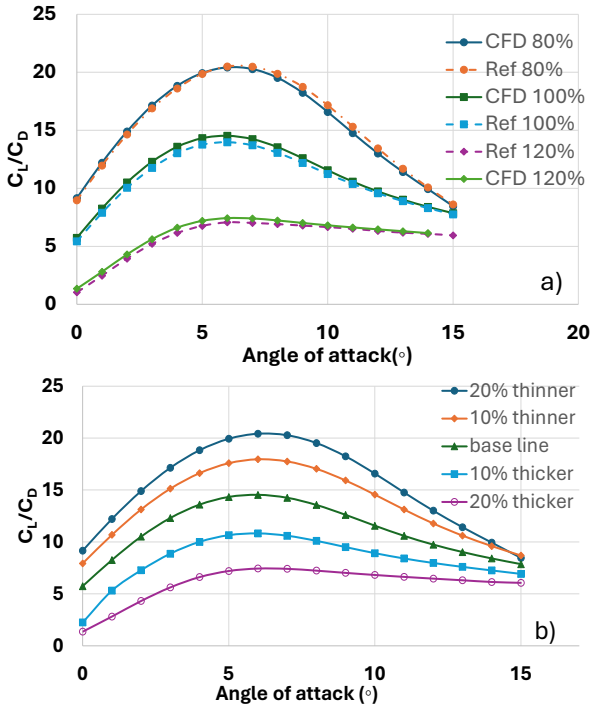

Fig. 8 a) Different of CFD result and Abdulkareem's result b) Effect of thickness on aerodynamic performance

demonstrate consistency with the reference work, showing that the thinner airfoil (80% thickness) increases the C_L/C_D ratio by 1.5 times compared to the original airfoil and by more than 3 times compared to the thicker airfoil (120% thickness).

This study also conducted simulations for various airfoil thicknesses to further understand how changes in thickness impact performance. The results, shown in Figure 8b, included thickness variations of 80%, 90%, 110%, and 120% of the S830 airfoil's base thickness. The maximum aerodynamic coefficient decreased as airfoil thickness increased, with the values for the five cases being 20.5, 17.96, 14.5, 10.8, and 7.43, respectively, all at a 6-degree angle of attack. Based on these results, the thickness can be selected according to the desired aerodynamic performance.

Figures 9a and 9b show the velocity distribution on profiles that are 20% thicker and thinner than the original size. Thicker profiles experience more severe flow separation, with the separation point occurring at about 40% of the chord length. In contrast, for thinner airfoils (20% thinner), this point shifts closer to the trailing edge, around 70% of the chord. Additionally, a thinner airfoil encounters less air resistance, reducing the C_D coefficient. However, thinner airfoils may suffer from decreased load-carrying capacity and stiffness of the turbine blades. Therefore, in the research and application of variable thickness for wind turbine airfoils, structural integrity must be prioritized to ensure reliable operation under harsh environmental conditions.

3.5 Ice accretion.

The US Aeronautics and Space Administration (NASA) very early studied the phenomenon of ice accretion on aircraft wings. The results showed a repeat of the accreted ice crystal shape for the wings NACA 0012 at -15 degrees Fahrenheit and a wind velocity of 150 mph (67.06 m/s) after 6 minutes (Jaiwon Shin *et al.,* 1992).

In Vietnam, where the Ice accretion can occur for airfoil, wind turbines are only encountered in highland areas and in winter. Due to the influence of climate change, the weather is becoming more and more extreme, so it is possible that this phenomenon will occur more often and in more locations. The specific location considered for the project is in Sapa. At an altitude of 1,600 meters, Sapa recorded the lowest temperature of -4.2°C (Hong Thao *et al.* 2016).

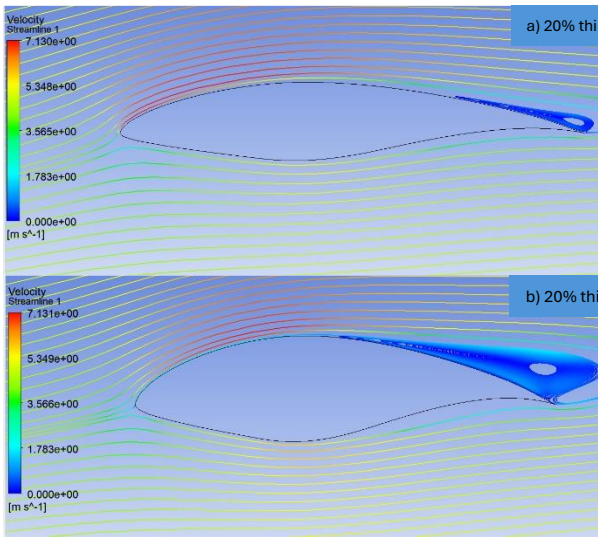

Fig. 9 Streamline air velocity in airfoil a) with 20% thinner b) with 20% thicker

Table 3
Conditions of Ice accretion models

Parameters	Airfoil	
	NACA 0012	S830
Chord (m)	0.533	0.09
Angle of attack (◦)	4	6
Reynold number	2.88 E6	2.88 E6
Droplet diameter(μm)	20	20
Number of shots	6	6
Wind velocity (m/s)	67.06	5
LWC (g/m3)	1	0.25
Temperature (°F)	-15	-3
Time (min)	6	90

First, the ice accretion model's correctness is tested in this study using NASA's case number NACA 0012. Next, the conditions of ice accretion on airfoil S830 in Sapa climatic conditions will be examined (Table 3).

The ice accretion from the ICE3D module was analyzed and compared to NASA's experimental results (Figure 10a) (Jaiwon Shin et al., 1992). With a total deposition time of 6 minutes, the simulation utilizes a multi-shot technique, with each shot lasting 1 minute. A comparison between the simulation and experimental results will help assess the appropriateness of this 1-minute time interval for each shot. All six shots demonstrate good convergence, requiring around 130 iterations in FLUENT to reach a residual of 10^{-5}. The results regarding the shape of ice accretion indicate that ice primarily accumulates on the front part of the airfoil, specifically at the leading edge. In addition to this area, a very thin layer of ice forms around the airfoil, although it is not significant. The portions of the airfoil surface that come into contact with areas of high-water density experience rapid accretion. Conversely, the rear section, including the belly and tail of the airfoil, which is in contact with regions of very low water density (approximately 0 g/m³), shows minimal signs of ice accumulation.

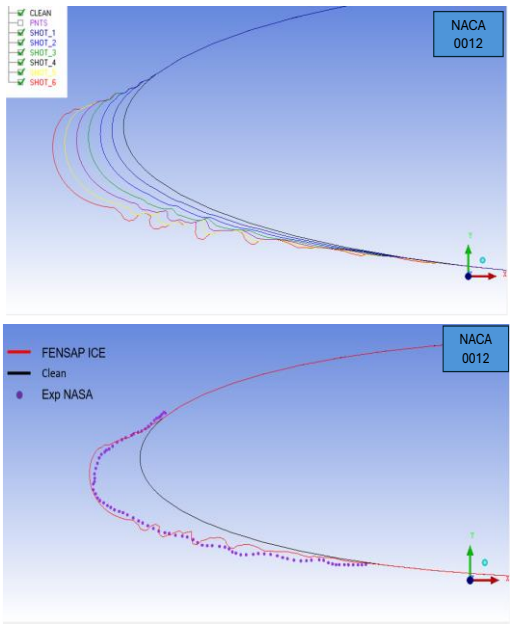

Fig. 10 a) Ice accretion for shot NACA 0012 b) FENSAP-ICE results vs NASA results

The largest size and curve shape of the ice accumulation in both the current simulation and NASA's experimental results show a high degree of similarity (Figure 10b). The convex edge in the lower half, after an extended period, takes on a pile-shaped tooth form. This observation is also documented in NASA's experimental report. The initial simulation demonstrated that the FENSAP-ICE model's accuracy, when compared to NASA experiments, was relatively good. Consequently, this method was further applied to predict ice formation on an actual wind turbine using the S830 airfoil located in Sapa.

The simulation results for the ice accretion phenomenon on the S830 airfoil are shown in Figure 11. The LWC distribution is shown in (Figure 11a). At the leading-edge position, there are sharp-shaped accretions. Ice accretion is concentrated in the convex profile of the wing tips because these areas have a high LWC density, and the concave parts almost do not occur. The accretion profile in the lower half of the airfoil will eventually develop a sawtooth shape after prolonged exposure. This phenomenon has also been documented in the NASA experimental report of NACA0012 (Jaiwon Shin *et al.,* 1992). The sawtooth pattern is indicative of the uneven buildup of ice, which can significantly affect the aerodynamic characteristics of the airfoil.

Figure 11b shows the ice accretion after 90 minutes in six consecutive shots of the S 830 wing profile. Due to the lower velocity and water density in the calculation area, the ice accretion time on the S830 airfoil is significantly longer than that in the NACA 0012 case. Consequently, the time allocated per shot has been adjusted to 15 minutes. In comparison with the

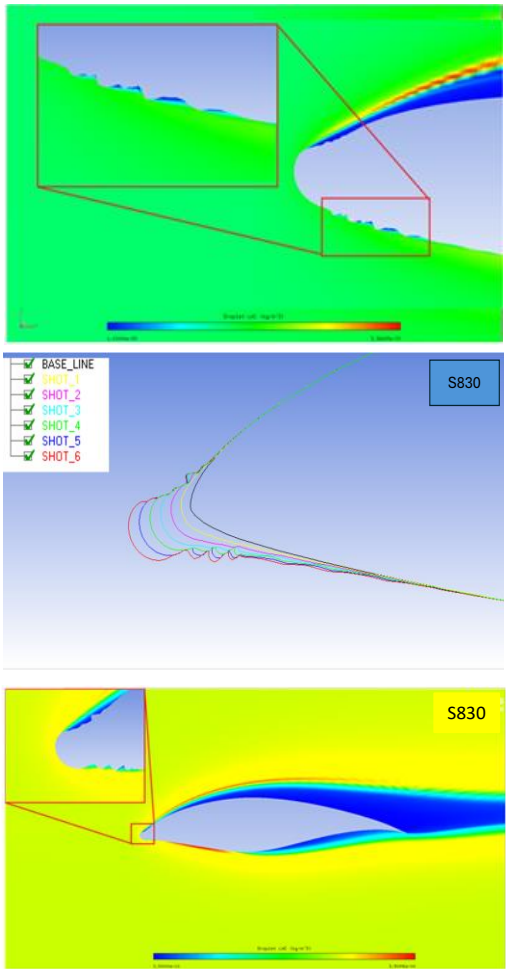

Fig. 11: a) LWC distribution after 6 minutes, b) Ice accretion for shot airfoil S830 and c) LWC contribution S830 after 90 minutes

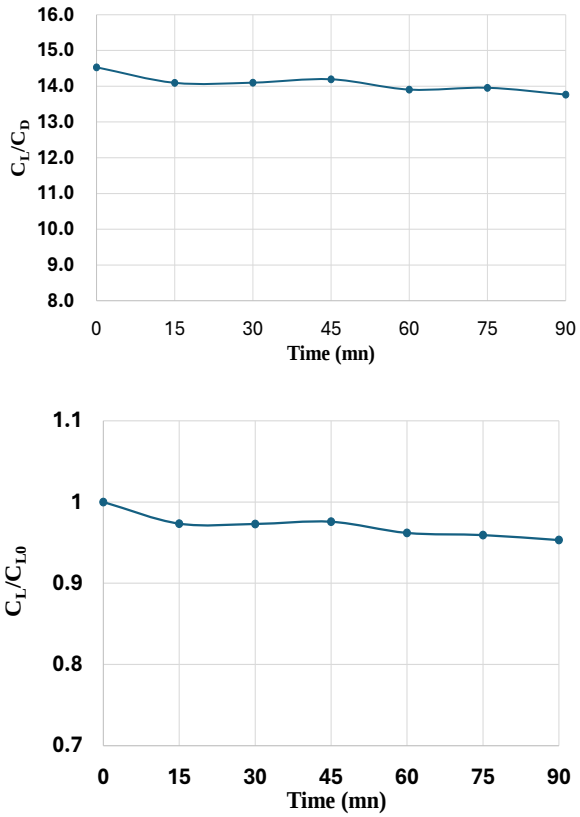

Fig. 12 a) Change of C_L/C_D vs time b) Change of C_L vs time

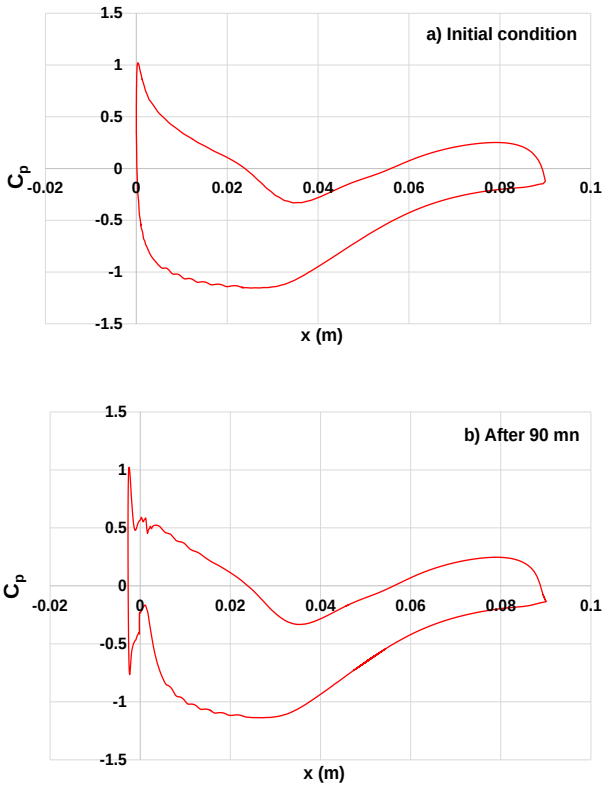

Fig. 13 Change of C_P

accretion rate observed in the NACA 0012 case, the largest ice accretion size based on the average chord (I/ $C_{average}$) has been calculated using the same methodology and is displayed on the chart. The results indicate that the I/C value for shot 1 is approximately 0.55%, which is similar to the I/ $C_{average}$ of the NACA 0012 case at 0.52%. However, due to the significant growth rate during the shots, the I/ $C_{average}$ value for the S830 airfoil case reaches 0.64%.

Figure 11c depict the shape of the accretion ice for each shot. The bulk and structure of the ice accumulation are strikingly similar at both the top and bottom sites. The water density distribution plots indicate that the trailing edge is exposed to a high-water density airstream, which accounts for the significant ice accretion observed compared to the NACA 0012 case. Additionally, the sawtooth pattern of accretion is present both above and below the leading edge. The plots reveal that the indentations are in regions with low water density and velocity.

Figure 12a illustrates the change in aerodynamic efficiency C_L/C_D of the S830 airfoil after after 6 shots of ice deposition. The aerodynamic efficiency coefficient shows a slight decline over time, decreasing by 4.68% from the initial value of 14.53 to 13.76 after 90 minutes. When evaluating the lift coefficient separately, this phenomenon results in a reduction of 5.25% compared to the initial value, as shown in Figure 12b. This reduction is not significant when compared to other scientific publications on the same topic, where similar trends can be observed. For instance, in the study by Virk *et al.* (2010), both the duration and size of the ice accretion were considerably larger in relation to the chord length than in this case, yet they recorded only a decrease of about 10% compared to the initial airfoil performance. Both figures indicate that the reduction in efficiency is most pronounced during the first shot, with subsequent shots showing a gradual decrease in the rate of efficiency loss.

Not only does the size of the airfoil chord change, but the deposited ice also creates sawtooth shapes below the leading edge. These structures alter the airfoil's inherent aerodynamic characteristics. Specifically, at the sawtooth positions, low-velocity regions with high pressure are generated, which subsequently affects the CP pressure coefficient. Pressure coefficient (C_P) plot for cleaning and accretion after 90 minutes is shown in Figure 13. The result shows that the leading edge is experiencing the biggest convergence that changes the airfoil size. This is indicated by a large C_P pressure coefficient exceeding the position x = 0 on the graph. Due to the impact of the saw-like formations, the pressure coefficient (C_P) above the new leading edge exhibits significant fluctuations, lacking a clear characteristic line or trend. The trailing edge also experienced a congestive phenomenon, so the characteristic line for the C_P coefficient also changed. Specifically, the C_P line of the airfoil after 90 minutes of concentrating at the end position is sharper in shape than the case for the original air foil.

4. Conclusion.

The paper presents a numerical analysis addressing the real-world challenge of wind turbine airfoil performance. The simulation results highlight the effects of angle of attack, airfoil thickness, Reynolds number, and ice accretion on the lift-to-drag ratio (C_L/C_D) of the airfoil. Firstly, the study determined the optimal angle of attack for each velocity scenario. At this optimal angle, the lift-to-drag coefficient (C_L/C_D) of the airfoil can be increased by more than twice compared to the case with a zero angle of attack. Specifically, at a wind speed of 5 m/s, the optimal angle of attack was found to be 6 degrees. At this angle, the C_L/C_D coefficient increased by approximately 250%

compared to a zero angle of attack, significantly enhancing the efficiency of the energy equipment. Wind speed also has a large effect on efficiency when changing the C_L/C_D coefficient. Next, this article also draws on the approach according to the Reynolds number definition to cover other factors of air flow while still ensuring the simplicity and economy of the method. The aerodynamic quality coefficient generally increases with the Reynolds number. As the Reynolds number rises, the optimal angle of attack gradually decreases. Additionally, the impact of varying thickness on turbine efficiency was examined. A thinner airfoil (80% of the original thickness) increases the C_L/C_D ratio by 1.5 times compared to the original airfoil and by over 3 times compared to a thicker airfoil (120% of the original thickness). However, implementing this solution requires a comprehensive study of structural issues to ensure the turbine's stable operation under varying environmental conditions. The study shows that FENSAP-ICE predicts the accretion of ice profiles well. This is shown in the condition test in the case of NACA 0012. Investigation of this phenomenon on the S830 airfoil shows a 5.25% decrease in C_L and a 4.68% decrease in C_L/C_D. Ice accretion alters the airfoil's dimensions and significantly impacts the pressure distribution and pressure coefficient (C_P). For a period of 90 minutes, the change in the lift factor does not have a big effect, but if the accretion takes place for a long time, this change can become large and adversely affect the operation of the turbine. Studies on longer periods of ice build-up as well as measures to limit ice build-up on turbine blades need further research.

Acknowledgment

This study is funded by Hanoi University of Science and Technology (HUST) under grant number T2023-PC-017. The authors are also grateful for the cooperation between Viettel Aerospace Institute and Hanoi University of Science for the support during this research.

Conflicts of Interest: The authors declare no conflict of interest.

References

Abdulkareem, O.A., Khudheyer, A.F., Abbas, A.S. (2021) Numerical Investigation of the Effect of Changing the Thickness of Airfoils used in Wind Turbines on the Lift to Drag Ratio. *IOP Conf. Series: Materials Science and Engineering* 1094, 012078; https://doi.org/10.1088/1757-899X/1094/1/012078

ANSYS CFX-19.1, ANSYS Inc, 2018.

Beabpimai, W., and Chitsomboon, T. (2019) Numerical Study of Effect of Blade Twist Modifications on the Aerodynamic Performance of Wind Turbine. *International Journal of Renewable Energy Development,* 8(3), 285-292. https://doi.org/10.14710/ijred.8.3.285-292

Belamadi, R., Djemili, A., Ilinca, A., Mdouki, R. (2016) Aerodynamic performance analysis of slotted airfoils for application to wind turbine blades. *J. Wind Eng. Ind. Aerodyn* 151, 79–99; http://dx.doi.org/10.1016/j.jweia.2016.01.011

Cai, M., Abbasi, E., Arastoopour, H. (2012) Analysis of the Performance of a Wind-Turbine Airfoil under Heavy-Rain Conditions Using a Multiphase Computational Fluid Dynamics Approach. Industrial & *Engineering Chemistry Research* 52, 3266−3275; https://dx.doi.org/10.1021/ie300877t

Cohan, A.D., Arastoopour, H. (2016) Numerical simulation and analysis of the effect of rain and surface property on wind-turbine airfoil performance. *International Journal of Multiphase Flow* 81, 46–53; http://dx.doi.org/10.1016/j.ijmultiphaseflow.2016.01.006

Geyer, T.F., Moreau, D.J., A study of the effect of airfoil thickness on the tonal noise generation of finite, wall-mounted airfoils. *Aerospace Science and Technology* 115, 106768; https://doi.org/10.1016/j.ast.2021.106768

Ghiasi, P., Najafi, G., Ghobadian, B., Jafari, A. (2021) Analytical and Numerical Solution for H-type Darrieus Wind Turbine Performance at the Tip Speed Ratio of Below One. *Int. Journal of Renewable Energy Development*, 10(2), 269-281 https://doi.org/10.14710/ijred.2021.33169

Gudmundsson, S., BScAE, MScAE, FAA DER (ret.). (2014) Performance – Cruise. *General Aviation Aircraft Design* 847-894; http://dx.doi.org/10.1016/B978-0-12-397308-5.00019-2

Guenoupkati, A., Salami, A. A., Bokovi, Y., Koussetou, P. X., & Ouedraogo, S. (2023). Estimating mixture hybrid Weibull distribution parameters for wind energy application using Bayesian approach. *International Journal of Renewable Energy Development, 12*(5), 902-912. https://doi.org/10.14710/ijred.2023.54452

Hassoine, M.A., Lahlou, F., Addaim, A., Madi, A.A. (2022) Improved Evaluation of The Wind Power Potential of a Large Offshore Wind Farm Using Four Analytical Wake Models. *International Journal of Renewable Energy Development*, 11(1), 35-48. https://doi.org/10.14710/ijred.2022.38263

Horcas, S.G., Madsen, M.H.A., Sorensen, N.N., Zahle, F., Barlas, T. (2022) Influence of the installation of a trailing edge flap on the vortex induced vibrations of a wind turbine blade, *Journal of Wind Engineering & Industrial Aerodynamics*, 105-118. https://doi.org/10.1016/j.jweia.2022.105118

Hong, T., Phung, T. (2016). Sa Pa is historically cold -4.2 degrees Celsius, Hanoi temperature is the lowest in 39 years. *Tuoi Tre Online Newspaper,* https://tuoitre.vn/sa-pa-ret-ky-luc-42-do-c-nhiet-do-ha-noi-tiep-tuc-giam-1043953.htm. (accessed April 30, 2024)

Lee, S. L., & Shin, S. J. (2021). Structural design optimization of a wind turbine blade using the genetic algorithm. *Engineering Optimization*, *54*(12), 2053–2070. https://doi.org/10.1080/0305215X.2021.1973450

Le, T.H.H, Huynh, T.P., Nguyen, D.A., & Nguyen, N.H. (2023). Simulation of Drag Crisis Phenomena Over a 3D Teardrop-shaped Body, *Journal of Aeronautics, Astronautics and Aviation*, 55(2), 105 – 118. https://doi.org/10.6125/JoAAA.202306_55(2).01

Le, T. T. N., Vu, D. Q., Vu, D. Q. (2023) Random Vibration Fatigue Analysis of a Small Horizontal Axis Wind Turbines Blade NREL S809, *Journal of Aeronautics, Astronautics and Aviation*, 55(3), 367 – 378 ; https://doi.org/10.6125/JoAAA.202309_55(3).07

Le T.T.N, Vu D.Q., Vu D. Q. (2022). Fluid-Structure Interaction Analysis of a Small Horizontal Axis Wind Turbine Blade NREL S809, *The proceeding of the 6th Southeast Asia Workshop on Aerospace Engineering*, p394-409,

Mamouri, A.R., Khoshnevis, A.B., Lakzian, E. (2019) Entropy generation analysis of S825, S822, and SD7062 offshore wind turbine airfoil geometries. *Ocean Engineering* 173, 700–715; https://doi.org/10.1016/j.oceaneng.2018.12.068

Makkonen, L., Zhang, J., Karlsson, Tiihonen, M. (2018) Modelling the growth of large rime ice accretions, *Cold Regions Science and Technology* 151, 133-137, https://doi.org/10.1016/j.coldregions.2018.03.014

Mohamed, M.H. (2019) Criticism study of J-Shaped darrieus wind turbine: Performance evaluation and noise generation assessment. *Energy* 177, 367e385; https://doi.org/10.1016/j.energy.2019.04.102

Merino-Martínez, R., Pieren, R., Schäffer, B. (2021) Holistic approach to wind turbine noise: From blade trailing-edge modifications to annoyance estimation. *Renewable and Sustainable Energy Reviews* 148, 111285; https://doi.org/10.1016/j.rser.2021.111285

Mereu, R., Passoni, S., Inzoli, F. (2019) Scale-resolving CFD modeling of a thick wind turbine airfoil with application of vortex generators: Validation and sensitivity analyses. *Energy* 187, 115969; https://doi.org/10.1016/j.energy.2019.115969

Mohamed, E.A.E.A., Abdellatif, O.E., Osman, A.M. (2015) Numerical Investigation of the Performance of Twisted and Untwisted Blades for Small Horizontal axis Wind Turbines. *ERJ– Faculty of Engineering at Shoubra* 25(1).

Mohamed, E.A.E.A., Abdellatif, O.E., Osman, A.M. (2021) Experimental and numerical investigation into the effect of different blade configurations on performance of small-scale wind turbines. *Energy Reports* 7, 138–143; https://doi.org/10.1016/j.egyr.2021.06.025

Mrigua, K., Toumi, A., Zemamou, M., Ouhmmou, B., Lahlou, Y., Aggour, M. (2020) CFD Investigation of a New Elliptical-Bladed Multistage Savonius Rotors. *International Journal of Renewable Energy Development*, 9(3), 383-392. https://doi.org/10.14710/ijred.2020.30286

Navin kumar, B., Rajendran, S., Vasudevan, A., Balaji, G. (2020) Aerodynamic braking system analysis of horizontal axis wind turbine using slotted airfoil. *Materials Today*. https://doi.org/10.1016/j.matpr.2020.06.334

Orosa, J. A., García-Bustelo, E. J., & Oliveira, A. C. (2012). An Experimental Test of Low-Speed Wind Turbine Concentrators. *Energy Sources, Part A: Recovery, Utilization, and Environmental Effects*, *34*(13), 1222–1230. https://doi.org/10.1080/15567031003773312

Rana, D., Patel, S., Onkar, A. K., & Manjuprased, M. (2011), Time Domain Simulation of Airfoil Flutter Using Fluid Structure Coupling Through FEM Based CFD Solver. *Symposium on Applied Aerodynamics and Design of Aerospace Vehicle,* https://api.semanticscholar.org/CorpusID:73583433

Rahman, M. R., Rahman, M. M., & Akter, R. (2023). Exploring the link between green energy, CO2 emissions, exchange rate and economic growth: Perspective from emerging South Asian countries. *International Journal of Renewable Energy Development, 12*(5), 930-941. https://doi.org/10.14710/ijred.2023.53168

Shah, H., Bhattarai, N., Mathew, S., Lim, C.M. (2012) Low Reynolds Number Airfoil for Small Horizontal Axis Wind Turbine Blades. *Innovations for Sustainable and Secure Energy* 21-23. https://www.jstor.org/stable/43749658

Shin, J., Bond., T.H. (1992) Results of an Icing Test on a NACA 0012 Airfoil in the NASA Lewis Icing Research Tunnel. *30th Aerospace Sciences Meeting and Exhibit.* https://ntrs.nasa.gov/api/citations/19920005833/downloads/19920005833.pdf

Shalby, M., Salah, A. A., Matarneh, G. A., Marashli, A., & Gommaa, M. R. (2023). An investigation of a 3D printed micro-wind turbine for residential power production. *International Journal of Renewable Energy Development, 12*(3), 550-559. https://doi.org/10.14710/ijred.2023.52615

Shiehab, T.H., Lina, S.Y., Yang, F.S., Chen, Y.T. (2016), Aerodynamic Effects of Unsteady Blade-Tower Interaction, *Journal of Aeronautics, Astronautics and Aviation*, Vol.48, No.4, pp.289 – 296. https://doi.org/10.6125/16-1201-915

Tian, K., Song, L., Jiao, X., Feng, R., Chen, Y., & Tian, R. (2021). Aeroelastic stability analysis and failure damage evaluation of wind turbine blades under variable conditions. *Energy Sources, Part A: Recovery, Utilization, and Environmental Effects*, 1–18. https://doi.org/10.1080/15567036.2021.1924320

Velázquez, M.T., Carmen, M.V.D., Francis, J.A., Pacheco, L.A.M., Eslava, G.T. (2014) Design and Experimentation of a 1 MW Horizontal Axis Wind Turbine. *Journal of Power and Energy Engineering* 2, 9-16; https://dx.doi.org/10.4236/jpee.2014.21002

Virk, M.S., Homola, M.C., Nicklasson, P.J. (2010) Effect of Rime Ice Accretion on Aerodynamic Characteristics of Wind Turbine Blade Profiles. *Wind Engineering* 34(2), 207–218. https://doi.org/10.1260/0309-524X.34.2.207

Vu D. Q., Le T. T, N., Nguyen V. H. (2022), Structural Durability Analysis of Offshore Wind Turbine Tower with Monopile Foundation According to ICE 61400 Standards, *The AUN/SEED-Net Joint Regional Conference in Transportation, Energy, and Mechanical Manufacturing Engineering*, 1150–1158, https://doi.org/10.1007/978-981-19-1968-8_96

Xiong Liu, Cheng Lu, Shi Liang, Ajit Godbole, Yan Chen (2015), Vibration-induced aerodynamic loads on large horizontal axis wind turbine blades, *Applied Energy*, https://doi.org/10.1016/j.apenergy.2015.11.080

Ye, X., Hu, N., Zheng, N., Li, C. (2023) Numerical study on aerodynamic performance and noise of wind turbine airfoils with serrated gurney flap. *Energy*, 262(2), 125574; https://doi.org/10.1016/j.energy.2022.125574

Zhang, X., Wang, Z., Li, W., Wang, Z., Bocian, M. (2023) Design optimization of a blunt trailing-edge airfoil for wind turbines under rime ice conditions. *Alexandria Engineering Journal* 65, 887-896; https://doi.org/10.1016/j.aej.2022.09.054

Zhang, Y., Avallone, F., Watson, S. (2022) Wind turbine blade trailing edge crack detection based on airfoil aerodynamic noise: An experimental study. *Applied Acoustics* 191, 108668; https://doi.org/10.1016/j.apacoust.2022.108668